Modal and nonmodal stability analysis for an electrified falling film

Arghya Samanta*

Department of Applied Mechanics, Indian Institute of Technology Delhi, Hauz Khas, New Delhi 110016, India

(Received 14 November 2022; revised 24 February 2023; accepted 12 April 2023; published 27 April 2023)

We have performed the modal and nonmodal stability analyses of a gravity-driven three-dimensional viscous incompressible fluid flowing over an inclined plane in the presence of a uniform electric field acting normal to the plane at infinity. The time evolution equations are derived for normal velocity, normal vorticity, and fluid surface deformation, respectively, and solved numerically by using the Chebyshev spectral collocation method. The modal stability analysis demonstrates the existence of three unstable regions for the surface mode in the wave number plane at the lower value of the electric Weber number. However, these unstable regions coalesce and magnify as the electric Weber number rises. By contrast, there exists only one unstable region for the shear mode in the wave number plane, which attenuates slightly with an increase in the value of the electric Weber number. But both the surface and shear modes are stabilized in the presence of the spanwise wave number, where the long-wave instability shifts towards the finite wavelength instability as the spanwise wave number rises. On the other hand, the nonmodal stability analysis reveals the existence of transient disturbance energy growth, the maximum value of which intensifies slightly with an increase in the value of the electric Weber number.

DOI: 10.1103/PhysRevE.107.045105

I. INTRODUCTION

Studies of the stability of viscous films have generated enormous interest in the research field because of their variety of applications in mechanical, chemical, and technological industries. As such studies have fundamental importance in fluid mechanics, numerous researchers are deeply involved in this field. Some of the pioneering research work on the stability of viscous films includes the following: Benjamin [1] and Yih [2] first initiated the study of long-wave instability subjected to an infinitesimal disturbance on the surface of a viscous film flowing down an inclined plane without an electric field and determined the critical Reynolds number for the onset of the surface mode instability, which is a function of the angle of inclination. They reported that the unidirectional parallel flow with a flat surface becomes unstable to two-dimensional infinitesimal disturbances if the Reynolds number exceeds the critical value. After that, the same flow problem was revisited by Lin [3] and Bruin [4] to decipher the shear mode instability, which, in fact, dominates over the surface mode instability at the high Reynolds number regime when the inclination angle is sufficiently small. However, the effect of surface tension was not discussed in their studies. This gap was filled in the research work of Chin *et al.* [5] and Floryan *et al.* [6]. As they discussed, the critical Reynolds number for the onset of the shear mode instability has a nonmonotonic behavior as the surface tension increases. Chang *et al.* [7] investigated the nonlinear evolution of the surface mode instability for a vertically falling film. Using three-dimensional Navier-Stokes equations based on the boundary layer approximation, they showed that the most unstable disturbance is the two-dimensional one. Reviews of this topic have been provided by Chang [8], Oron *et al.* [9], and Craster and Matar [10]. In this context, there is already evidence that the shear flow exhibits a transient disturbance energy growth phenomenon when the Reynolds number lies in the subcritical regime [11–13]. Actually, the idea of the existence of transient disturbance energy growth for a shear flow emerged to explain the discrepancy between the results procured from the eigenvalue analysis, energy analysis, and experiment [13]. According to Schmid and Henningson [13], the reason is the non-normal nature of the eigenvalue operator, which renders a set of nonorthogonal eigenfunctions, and their superposition yields a transient amplification. As a consequence, the critical Reynolds number for the onset of the shear mode instability differs from that determined from the modal stability analysis or eigenvalue analysis. Hence, the nonmodal stability analysis is imperative for a flow configuration whose eigenvalue operator is not normal. The existence of transient disturbance energy growth for a gravity-driven falling film with a free surface without an electric field was reported in the research work of Olsson and Henningson [14] and Samanta [15,16] because such flows are also susceptible to shear mode instability in the high Reynolds number regime. For this reason, we are inspired to explore the nonmodal stability analysis for the gravity-driven electrified falling film.

Recently, many studies [17–20] have been carried out to decipher the effect of an electric field on the surface mode instability of falling viscous films. Actually, these studies have been motivated by the fact that the presence of an electric field introduces an additional Maxwell stress along with the existing hydrodynamic stress at the fluid-air interface, where the fluid is treated as a perfect conductor and the air surrounding the fluid surface is treated as a perfect dielectric. In particular, Kim *et al.* [17] explored the flow of a viscous fluid down

*arghya@am.iitd.ac.in

a wall in the framework of the lubrication approximation and developed a time evolution equation for the fluid surface height, $h(x,t)$. The linear stability analysis was accomplished. Later, an experimental validation of Kim's result was reported by Griffing *et al.* [18]. The nonlinear surface wave dynamics for an electrified falling film was scrutinized by Gonzalez and Castellanos [19] and Tseluiko and Papageorgiou [21] based on the Benney-type surface evolution equation, which contains a nonlocal term involving the electric potential. It was reported that the presence of an electric field exhibits a destabilizing impact on the surface mode instability. However, it is worth reporting here that they ignored the effect of the induced magnetic field by assuming low conductivities so that the electrostatic approximation of Maxwell's equations prevailed. Furthermore, the influence of electrostriction force was neglected and there was no electric field inside the fluid as it was treated as a perfect conductor. In addition, they assumed that the electric conductivity and the electric permittivity of the fluid were constants. Finally, they considered that the charge relaxation timescale is small compared to the dynamical timescale, allowing them to apply continuity of current across the fluid-air interface [22–24]. As the Benney-type surface evolution equation possesses an unphysical blowup property, the weighted residual method [25] was implemented by Wray *et al.* [26] to derive a coupled system of evolution equations for the local film thickness, local flow rate, and two subsidiary fields which measure the distortion of the streamwise velocity from the parabolic base flow velocity. Their numerical result demonstrated a good agreement with that obtained from the direct numerical simulation of the Navier-Stokes equations. Later, Rohlfs *et al.* [27] conducted an experimental study to examine the effect of electrostatic forces on the nonlinear waves evolved on the surface of a falling film. They demonstrated that the wave peak height is increased and decreased in different regions of the wave. The electrostatic field induced instability, morphology, and pattern formation on the surface of a thin film confined between two electrodes can be found in the work of Verma *et al.* [28]. The results were produced for both spatially homogeneous and heterogeneous electric fields. A hexagonal packing of liquid columns is formed if a spatially homogeneous electric field is applied, whereas a spatial variation of the electrostatic field produces locally ordered aligned patterns. As the insoluble surfactant has a stabilizing influence [29] and the electric field has a destabilizing influence on the surface mode instability, Blyth [30] investigated the combined effect of the insoluble surfactant and electric field on the surface mode instability of a viscous film flowing down an inclined plane. He first discovered an inertialess instability in the finite wave number regime, which intensifies as the electric Weber number increases. Samanta [31] studied the shear mode instability of an electrified falling film. As discussed by Samanta, the electric field suppresses the shear mode instability at low values of the inclination angle. After that, Samanta [32] examined the linear spatiotemporal instability for the same flow problem. He found that the four spatial branches obtained from the Orr-Sommerfeld equation lose their spatial symmetry if the effect of an electric field is introduced in the flow configuration. Recently, the binary interaction between the solitary pulses and their bound state form was discovered by Blyth *et al.* [33] for an electrified falling film. A detailed review of this topic can be found in Refs. [22,24,34].

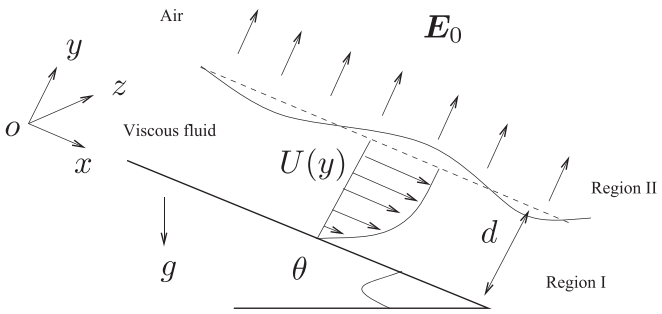

FIG. 1. A sketch of a three-dimensional gravity-driven electrified viscous falling film.

It is worth noting that the above studies were conducted on the two-dimensional electrified viscous falling films. More specifically, most of the studies only carried out the modal stability analysis for the two-dimensional disturbances, where the effect of the spanwise wave number was negated. It seems that they used Squire's theorem, which prevails in the modal stability analysis, because, using Squire's transformation, one can demonstrate that the two-dimensional disturbance is linearly more unstable than the three-dimensional ones. However, such a statement cannot be applied in the nonmodal stability analysis because only spanwise disturbance provided the largest transient disturbance energy growth when compared to disturbances that include both the streamwise and spanwise wave numbers [35]. The analytical derivation of Squire's theorem for the electrified falling film is further provided in Appendix A. Moreover, there is no information about the nonmodal stability analysis for the electrified falling film. To fill these gaps available in the literature, we are motivated to study the modal and nonmodal stability analyses for an electrified falling film corresponding to the three-dimensional disturbances of arbitrary wave numbers.

II. EQUATIONS OF MOTION

Consider the flow of a gravity-driven viscous incompressible fluid down an inclined plane with a slope angle θ with the horizontal and a uniform electric field $\boldsymbol{E}_0$ acting normal to the plane at infinity. In fact, this is similar to the electrified falling film model proposed by Tseluiko and Papageorgiou [21], but the flow configuration is three dimensional rather than the two-dimensional one. The sketch of the flow model is shown in Fig. 1. Suppose that $y = h(x,z,t)$ denotes the height of the disturbed fluid surface, and d is the height of the undisturbed fluid surface from the plane in the cross-stream direction when the fluid flow is unidirectional and parallel. The Cartesian coordinate system is used to describe the current flow configuration, where the origin is located at the inclined plane and the axes x, y, and z are placed along the streamwise, cross-stream, and spanwise directions, respectively. The physical properties of the fluid, such as density ρ, dynamic viscosity μ, and surface tension σ, are constants for a given fluid. Suppose the viscous fluid occupying region I is a perfect conductor, and the air surrounding the fluid surface in region II is a perfect

dielectric with a permittivity ε_a (see Fig. 1). Here, the inclined plane is considered as an infinite electrode and it is grounded. Therefore, it possesses a zero voltage potential. The three-dimensional flow of the Newtonian viscous incompressible fluid is governed by the mass conservation and momentum equations [36],

$$\partial_{x_i} u_i = 0,\ i = 1, 2, 3, \tag{1}$$

$$\rho(\partial_t u_i + u_j \partial_{x_j} u_i) = -\partial_{x_i} p + \mu \partial_{x_j x_j} u_i + \rho g_i,\ i, j = 1, 2, 3, \tag{2}$$

where u_1, u_2, and u_3 are, respectively, the velocity components in the streamwise, cross-stream, and spanwise directions, and p is the pressure of the fluid. Here, $(g_1, g_2, g_3) = (g\sin\theta, -g\cos\theta, 0)$ are the components of the gravitational acceleration. In order to avoid any confusion and for the sake of mathematical simplicity, we shall assume $u_1 = u$, $u_2 = v$, $u_3 = w$, $x_1 = x$, $x_2 = y$, and $x_3 = z$. Now we introduce the electric potential Φ, which can be obtained from the electric field $\boldsymbol{E}$ with the help of the electrostatics approximation $\boldsymbol{E} = -\nabla\Phi$, i.e., the electric field $\boldsymbol{E}$ is irrotational ($\nabla \times \boldsymbol{E} = 0$). Furthermore, in electrostatics, the Gauss divergence law ($\nabla \cdot \boldsymbol{E} = 0$) in the dielectric air medium leads to the Laplace equation in terms of the electric potential Φ,

$$\nabla^2\Phi = \partial_{x_i x_i}\Phi = 0,\ i = 1, 2, 3. \tag{3}$$

The above governing equations are closed by the following boundary conditions:

(i) At the rigid inclined plane, $y = 0$, the velocity components of the fluid must satisfy no-slip and no-penetration boundary conditions,

$$u_i = 0,\ i = 1, 2, 3. \tag{4}$$

(ii) At the disturbed fluid-air interface, $y = h(x, z, t)$, an additional Maxwell stress is generated due to the presence of the normal electric field $\boldsymbol{E}$ along with the usual hydrodynamic stress, and their balance results in the tangential stress and normal stress boundary conditions [21,30,31,37,38],

$$\tau_{ij} n_j t_i^1 = 0,\ \tau_{ij} n_j t_i^2 = 0,\ i, j = 1, 2, 3, \tag{5}$$

$$\tau_{ij} n_i n_j = \sigma\kappa,\ i, j = 1, 2, 3, \tag{6}$$

where κ is the curvature of the fluid-air interface [36]. Here, (t_1^1, t_2^1, t_3^1) and (t_1^2, t_2^2, t_3^2) are the components of the unit tangent vectors in the streamwise and spanwise directions, and (n_1, n_2, n_3) are the components of the unit normal vector at the fluid-air interface [15,16,36]. The combined stress tensor τ_{ij} at the fluid-air interface can be written from the constitutive relations of region I and region II as [21,24,30,38,39]

$$\tau_{ij} = \tau_{ij}^{\mathrm{I}} - \tau_{ij}^{\mathrm{II}} = -p\delta_{ij} + \mu(\partial_{x_j} u_i + \partial_{x_i} u_j) + p_a\delta_{ij} - \varepsilon_a\left(E_i E_j - |\boldsymbol{E}|^2\frac{\delta_{ij}}{2}\right),\ i, j = 1, 2, 3, \tag{7}$$

where $\tau_{ij}^{\mathrm{I}} = -p\delta_{ij} + \mu(\partial_{x_j} u_i + \partial_{x_i} u_j)$ is the fluid stress tensor and $\tau_{ij}^{\mathrm{II}} = -p_a\delta_{ij} + \varepsilon_a(E_i E_j - |\boldsymbol{E}|^2\frac{\delta_{ij}}{2})$, where the second term in the expression of τ_{ij}^{II} appears due to the Maxwell stress generated by the electric field [24,40]. Here, p_a is the ambient pressure, δ_{ij} is the Kronecker delta, and E_i are the components of the electric field at the fluid-air interface.

(iii) The time evolution of the fluid-air interface, $y = h(x, z, t)$, can be understood with the help of the kinematic boundary condition,

$$\partial_t F + u_i \partial_{x_i} F = 0, \tag{8}$$

where $F(x, y, z, t) = y - h(x, z, t)$.

(iv) As the fluid is a perfect conductor, there is no electric field inside the fluid. The electric field $\boldsymbol{E}$ is acting only in the normal direction to the fluid-air interface, and it has no component in the tangential directions at the fluid-air interface. Therefore, we must have

$$\partial_{x_i}\Phi t_i^1 = 0,\ \partial_{x_i}\Phi t_i^2 = 0,\ i = 1, 2, 3. \tag{9}$$

Hence, the electric potential Φ is constant at the fluid-air interface. We assume that the electric potential Φ is zero at the fluid-air interface, $y = h(x, z, t)$ [21,30,31,38].

(v) Finally, the electric potential Φ also satisfies the following condition at infinity, $y \to \infty$:

$$\partial_{x_i}\Phi = -E_0\delta_{i2},\ i = 1, 2, 3. \tag{10}$$

Since we are mainly interested in exploring the modal and nonmodal stability of the primary flow or base flow, it is essential to compute the solution of the unidirectional parallel flow with a constant fluid layer thickness, $y = d$, the so-called base flow. As a result, the governing equations (1)–(10) for the base flow are simplified into the following forms:

$$\mu\partial_{yy} u + \rho g\sin\theta = 0,\ \partial_y p + \rho g\cos\theta = 0,\ \partial_z p = 0, \tag{11}$$

$$\partial_{yy}\Phi = 0. \tag{12}$$

The above base flow governing equations are subjected to the following boundary conditions:

$$u = 0 \text{ at } y = 0, \tag{13}$$

$$\partial_y u = 0,\ p = p_a - \frac{\varepsilon_a}{2}(\partial_y\Phi)^2,\ \Phi = 0 \text{ at } y = d, \tag{14}$$

$$\partial_y\Phi = -E_0 \text{ at } y \to \infty. \tag{15}$$

The solution of the base flow governing equations (11)–(15) can be expressed as

$$\bar{U}(y) = \frac{\rho g d^2\sin\theta}{2\mu}\left(2\frac{y}{d} - \frac{y^2}{d^2}\right),\ \bar{V} = 0,\ \bar{W} = 0, \tag{16}$$

$$\bar{P}(y) = \rho g d\cos\theta\left(1 - \frac{y}{d}\right) + p_a - \frac{\varepsilon_a}{2}E_0^2, \tag{17}$$

$$\bar{\Phi}(y) = E_0 d\left(1 - \frac{y}{d}\right), \tag{18}$$

where variables with bar notation represent the base flow variables. It should be noted that the base flow pressure is explicitly dependent on the magnitude of the uniform electric field $\boldsymbol{E}_0$, and it decreases as the magnitude of the electric field $\boldsymbol{E}_0$ increases. However, the base flow velocity is independent of the magnitude of the electric field $\boldsymbol{E}_0$.

III. LINEARIZED PERTURBATION EQUATIONS

Before proceeding to the derivation of the linearized perturbation equations, we introduce the following nondimensional variables:

$$x^* = \frac{x}{d},\ y^* = \frac{y}{d},\ z^* = \frac{z}{d},\ u^* = \frac{u}{U_s},$$
$$v^* = \frac{v}{U_s},\ w^* = \frac{w}{U_s},\ t^* = \frac{tU_s}{d},$$
$$p^* = \frac{p}{\rho U_s^2},\ \Phi^* = \frac{\Phi}{E_0 d},\ h^* = \frac{h}{d},$$

where the thickness of the base flow, d, is preferred as the characteristic length scale, the fluid surface velocity of the base flow, $U_s = \frac{\rho g d^2 \sin\theta}{2\mu}$, is preferred as the characteristic velocity scale, $\rho {U_s}^2$ is preferred as the characteristic pressure scale, $\frac{d}{U_s}$ is preferred as the characteristic timescale, and $E_0 d$ is preferred as the characteristic scale for the electric potential. For our convenience, we have omitted the star symbol from the nondimensional variables in the subsequent mathematical formulations. Next, we impose an infinitesimal three-dimensional perturbation on the base flow and, consequently, each variable of the disturbed flow and disturbed electric potential can be decomposed as

$$u = \bar{U}(y) + u', \quad v = \bar{V} + v', \quad w = \bar{W} + w',$$
$$p = \bar{P}(y) + p', \quad \Phi = \bar{\Phi}(y) + \phi', \quad h = 1 + h',$$

where the variables with prime notation represent the perturbation variables. After nondimensionalizing, the linearized perturbation equations can be expressed as

$$\partial_x u' + \partial_y v' + \partial_z w' = 0, \tag{19}$$

$$\partial_t u' + U\partial_x u' + v'\partial_y U + \partial_x p' = \frac{(\partial_{xx} + \partial_{yy} + \partial_{zz})u'}{\mathrm{Re}}, \tag{20}$$

$$\partial_t v' + U\partial_x v' + \partial_y p' = \frac{(\partial_{xx} + \partial_{yy} + \partial_{zz})v'}{\mathrm{Re}}, \tag{21}$$

$$\partial_t w' + U\partial_x w' + \partial_z p' = \frac{(\partial_{xx} + \partial_{yy} + \partial_{zz})w'}{\mathrm{Re}}, \tag{22}$$

$$(\partial_{xx} + \partial_{yy} + \partial_{zz})\phi' = 0, \tag{23}$$

$$u' = 0,\ v' = 0,\ w' = 0 \text{ at } y = 0, \tag{24}$$

$$(\partial_y u' + \partial_x v' + h'\partial_{yy} U) = 0 \text{ at } y = 1, \tag{25}$$

$$(\partial_y w' + \partial_z v') = 0,\ \phi' - h' = 0 \text{ at } y = 1, \tag{26}$$

$$-p' + \frac{2\partial_y v'}{\mathrm{Re}} + \frac{2E_{We}\partial_y \phi'}{\mathrm{Re}} + \frac{\cos\theta h'}{\mathrm{Fr}^2} - \mathrm{We}(\partial_{xx} + \partial_{zz})h' = 0 \text{ at } y = 1, \tag{27}$$

$$\partial_t h' + U\partial_x h' = v' \text{ at } y = 1, \tag{28}$$

$$\partial_x \phi' = 0,\ \partial_y \phi' = 0,\ \partial_z \phi' = 0 \text{ at } y \to \infty, \tag{29}$$

where $\mathrm{Re} = \frac{\rho U_s d}{\mu}$ is the Reynolds number which compares inertia to the viscous force, $\mathrm{Fr} = \frac{U_s}{\sqrt{gd}}$ is the Froude number which compares inertia to the gravity force, $\mathrm{We} = \frac{\sigma}{\rho U_s^2 d}$ is the Weber number which compares the capillary force induced by the surface tension to inertia, and $E_{We} = \frac{\varepsilon_a E_0^2 d}{2\mu U_s}$ is the electric Weber number which compares the surface force induced by the electric field to the viscous force [21,30]. In particular, the dimensionless electric Weber number E_{We} appears in the normal stress boundary condition (27) at the fluid-air interface due to the jump between the Maxwell stress generated by the electric field and the normal stress of the viscous film. For example, in the case of a thin film of silicon oil DMS T12 at 25 °C with thickness $d = 10^{-3}$ m, density $\rho = 949$ kg/m^3, kinematic viscosity $\nu = \mu/\rho = 2.03 \times 10^{-5}$ m^2/s, and surface tension $\sigma = 0.0201$ N/m flowing down an inclined plane with slope angle $\theta = 4^\circ$, the magnitude of the electric Weber number is approximately 13.6, when the magnitude of the uniform electric field, E_0, is of the order of 10^6 V/m and permittivity $\varepsilon_a = 8.85 \times 10^{-12}$ C/(Vm) [27]. However, if the physical properties of the fluid are constants for a given inclination angle, the magnitude of the electric Weber number can be altered by varying the magnitude of the applied uniform electric field. The Weber number We can also be written in terms of the Kapitza number as

$$\mathrm{We} = \mathrm{Re}^{-5/3}\left(\frac{3}{2}\sin\theta\right)^{-1/3}\Gamma, \tag{30}$$

where $\Gamma = (\frac{3\rho\sigma^3}{g\mu^4})^{1/3}$ is the Kapitza number, which can be varied only by changing the physical properties of the fluid [6,41]. Furthermore, the Weber number can also be expressed in terms of the capillary number as $\mathrm{We} = 1/(\mathrm{Ca}\,\mathrm{Re})$, where $\mathrm{Ca} = \mu U_s/\sigma$ is the capillary number [30,42].

IV. TIME EVOLUTION EQUATIONS

To develop time evolution equations, we assume the solution of the linearized perturbation equations (19)–(29) in the normal mode form [43],

$$\begin{bmatrix} u'(x,y,z,t) \\ v'(x,y,z,t) \\ w'(x,y,z,t) \\ p'(x,y,z,t) \\ \phi'(x,y,z) \\ h'(x,z,t) \end{bmatrix} = \begin{bmatrix} \hat{u}(y,t) \\ \hat{v}(y,t) \\ \hat{w}(y,t) \\ \hat{p}(y,t) \\ \hat{\phi}(y) \\ \hat{h}(t) \end{bmatrix} \exp[i(\alpha x + \beta z)], \tag{31}$$

where the variables with "hat" notation are the amplitudes of the perturbation variables. Here, α and β are the streamwise and spanwise wave numbers. Next, our purpose is to evaluate the electric potential term remaining in the normal stress boundary condition (27). With the aid of the normal mode solution (31), the Laplace equation for the electric potential can be expressed as

$$(\partial_{yy} - k^2)\hat{\phi} = 0, \tag{32}$$

where $k = \sqrt{\alpha^2 + \beta^2}$ is the total wave number. The general solution of Eq. (32) is of the form

$$\hat{\phi}(y) = c_1 \exp[ky] + c_2 \exp[-ky], \tag{33}$$

where c_1 and c_2 are arbitrary constants to be determined. Using the boundary conditions for the electric potential, one

can obtain

$$\hat{\phi}(y) = \frac{\hat{h}\exp[-ky]}{\exp[-k]}. \tag{34}$$

Now we introduce the perturbation normal vorticity component $\Omega' = \partial_z u' - \partial_x w'$. Next, by eliminating the pressure terms from the perturbation momentum equations (20)–(22) and after doing some mathematical calculations, we obtain the time evolution equations for normal velocity and normal vorticity components,

$$(\partial_{yy} - k^2)\partial_t \hat{v} = \frac{1}{\mathrm{Re}}(\partial_{yy} - k^2)^2 \hat{v} - i\alpha[U(\partial_{yy} - k^2)\hat{v} - \partial_{yy}U\hat{v}], \tag{35}$$

$$\partial_t \hat{\Omega} = \frac{1}{\mathrm{Re}}(\partial_{yy} - k^2)\hat{\Omega} - i\alpha U\hat{\Omega} - i\beta\partial_y U\hat{v}, \tag{36}$$

where $\hat{\Omega} = (i\beta\hat{u} - i\alpha\hat{w})$ is the amplitude of the perturbation normal vorticity component. The associated boundary conditions can be reduced to the following forms:

$$\hat{v} = 0,\ \partial_y\hat{v} = 0,\ \hat{\Omega} = 0 \text{ at } y = 0, \tag{37}$$

$$(\partial_{yy} + k^2)\hat{v} - i\alpha\hat{h}\partial_{yy}U = 0 \text{ at } y = 1, \tag{38}$$

$$\partial_y\hat{\Omega} + i\beta\hat{h}\partial_{yy}U = 0 \text{ at } y = 1, \tag{39}$$

$$\partial_y\partial_t\hat{v} = \frac{1}{\mathrm{Re}}(\partial_{yy} - 3k^2)\partial_y\hat{v} - i\alpha U\partial_y\hat{v} - \left[\frac{\cos\theta}{\mathrm{Fr}^2} + k^2\mathrm{We} - \frac{2kE_{We}}{\mathrm{Re}}\right]k^2\hat{h} \text{ at } y = 1, \tag{40}$$

$$\partial_t\hat{h} = \hat{v} - i\alpha U\hat{h} \text{ at } y = 1. \tag{41}$$

The above system of time evolution equations for normal velocity, normal vorticity, and fluid surface deformation can be written into a temporal matrix initial value problem [15,16],

$$\mathcal{B}\partial_t\hat{q} = \mathcal{A}\hat{q}, \tag{42}$$

with initial condition $\hat{q}_0 = \hat{q}(t)|_{t=0}$. It should be useful to mention here that the above set of equations coincides with that of Olsson and Henningson [14] if the effect of the electric field is removed from the current flow configuration. Here, $\hat{q} = [\hat{v}, \hat{\Omega}, \hat{h}]^T$ is the column matrix of the flow variables, and the matrices $\mathcal{A}$ and $\mathcal{B}$ can be expressed as [13,14]

$$\mathcal{A} = \begin{bmatrix} \mathcal{L}_{os} & 0 & 0 \\ \mathcal{L}_c & \mathcal{L}_{sq} & 0 \\ 1 & 0 & -i\alpha U \end{bmatrix}, \quad \mathcal{B} = \begin{bmatrix} (\mathcal{D}^2 - k^2) & 0 & 0 \\ 0 & 1 & 0 \\ 0 & 0 & 1 \end{bmatrix}, \tag{43}$$

where $\mathcal{D}^2 = \partial_{yy}$ is the differential operator, $\mathcal{L}_{os} = \frac{1}{Re}(\partial_{yy} - k^2)^2 - i\alpha[U(\partial_{yy} - k^2) - \partial_{yy}U]$ is the Orr-Sommerfeld operator, $\mathcal{L}_c = -i\beta\partial_y U$ is the coupling operator, and $\mathcal{L}_{sq} = \frac{1}{Re}(\partial_{yy} - k^2) - i\alpha U$ is the Squire operator. It is worthwhile to report here that the coupling operator $\mathcal{L}_c$ plays an important role in the appearance of transient disturbance energy growth. However, we can see the presence of another coupling term between the normal velocity component and fluid surface deformation arising from the kinematic boundary condition (41). Here, the normal velocity and normal vorticity components are simply the cross-stream velocity and cross-stream vorticity components, and they are normal to the bounding plane. It should be noted that the coupling equation (41) is absent from the mathematical formulation for a plane Poiseuille flow because there is no deformed fluid surface. In particular, these coupling terms are responsible for the appearance of short-time disturbance energy growth if the eigenfunctions are nonorthogonal [11–16].

V. MODAL STABILITY ANALYSIS

In this section, we shall investigate the modal stability analysis of the infinitesimal disturbance superimposed on the base flow. To this end, we recast the time evolution perturbation equations into a generalized matrix eigenvalue problem by assuming the solution in the following form [44]:

$$\hat{q}(y,t) = \tilde{q}(y)\exp[-i\omega t], \tag{44}$$

where $\tilde{q} = [\tilde{v}, \tilde{\Omega}, \tilde{h}]^T$ is the column matrix, $\omega = \alpha c = \omega_r + i\omega_i$ is the angular frequency, and c is the complex wave speed of the infinitesimal disturbance. After substitution of Eq. (44) into the perturbation time evolution equation (42), one can obtain the generalized matrix eigenvalue problem,

$$\mathcal{A}\tilde{q} = -i\omega\mathcal{B}\tilde{q}, \tag{45}$$

where $i = \sqrt{-1}$ is the imaginary number. Obviously, the angular frequency ω is the eigenvalue of the generalized matrix eigenvalue problem (45). If at least one of the eigenvalues lies in the unstable upper-half plane ($\omega_i > 0$), one can perceive an exponential temporal growth of the infinitesimal disturbance. Otherwise, the infinitesimal disturbance will be linearly stable if all the eigenvalues lie in the stable lower-half plane ($\omega_i < 0$). Now the eigenvalue problem (45) is solved numerically with the help of the Chebyshev spectral collocation method [13]. A brief discussion of the Chebyshev spectral collocation method can be found in Appendix B. In order to check the accuracy of the numerical code, we first perform the convergence analysis. Following the works of Tilton and Cortelezzi [45] and Samanta [46], we compute the relative error defined by

$$E_N = \|\boldsymbol{\omega}_{N+1} - \boldsymbol{\omega}_N\|_2 / \|\boldsymbol{\omega}_N\|_2, \tag{46}$$

where $\|\cdot\|_2$ represents the L_2 norm. Here, $\boldsymbol{\omega}_N$ is the column vector of the 20 least stable eigenvalues, which are taken from the spectrum in the numerical computation of the relative error when the number of Chebyshev polynomials is N. Figure 2(a) demonstrates the variation of the relative error E_N as the number of Chebyshev polynomials rises. We can see that the relative error approximately saturates between the order of 10^{-6} and the order of 10^{-8} for $N \geqslant 100$ when $\mathrm{Re} = 10\,000$, $\alpha = 1$, $\beta = 0$, $\theta = 1^\circ$, $E_{We} = 1$, and $\Gamma = 4899$. Therefore, 100 Chebyshev polynomials will be sufficient to get accurate numerical results. Here, the above flow parameter values can be acquired for a water film at 20 °C with thickness $d = 0.01$ m, density $\rho = 1000\ \mathrm{kg/m^3}$, gravity $g = 9.81\ \mathrm{m/s^2}$, dynamic viscosity $\mu = 10^{-3}$ kg/(m s), and surface tension $\gamma = 72.8 \times 10^{-3}$ N/m flowing down an inclined plane with slope angle $\theta = 0.1^\circ$ [5]. According to the definition, the calculated value of the Reynolds number is approximately $\mathrm{Re} \approx 8560$. However, its value can be changed by varying the value of the viscous flat film layer thickness d when the values of the other flow parameters are fixed. It is noteworthy to point

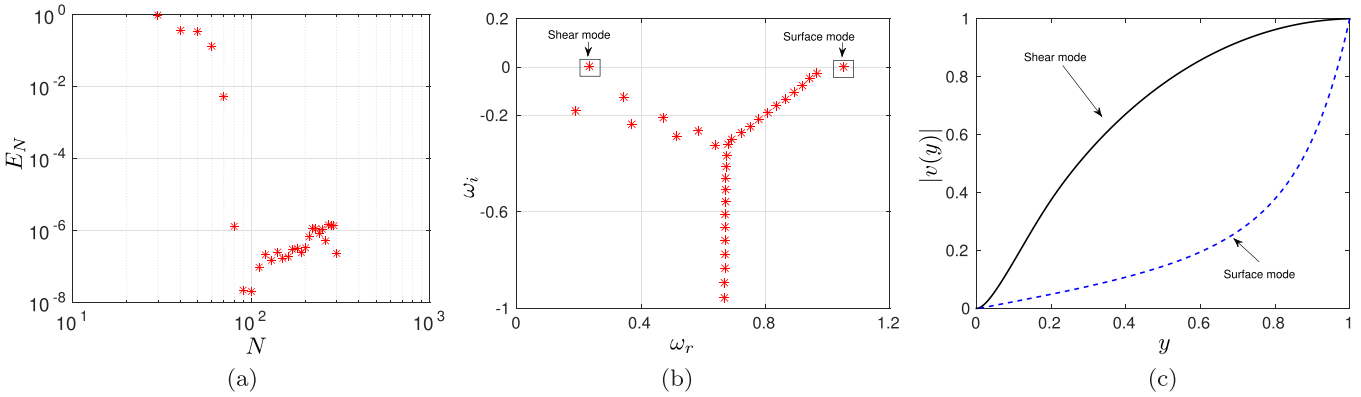

FIG. 2. (a) Variation of the relative error E_N as the number N of the Chebyshev polynomials alters. (b) Spectrum of the eigenvalue problem (45). (c) Variation of the absolute values of the normalized eigenfunctions $|v(y)|$ as a function of the cross-stream coordinate y. Solid and dashed lines represent the eigenfunctions for the shear mode and the surface mode, respectively. The flow parameter values are Re $= 10\,000$, $\alpha = 1$, $\beta = 0$, $\theta = 1^\circ$, $E_{We} = 1$, and $\Gamma = 4899$.

out that two dominant unstable modes are identified numerically, which are called the surface mode and the shear mode. More specifically, the surface mode is detected in both the low and high Reynolds number regimes, while the shear mode is detected only in the high Reynolds number regime with a low inclination angle. These two dominant modes are displayed in Fig. 2(b), where the spectrum of the eigenvalue problem (45) is depicted when Re $= 10\,000$, $\alpha = 1$, $\beta = 0$, $\theta = 1^\circ$, $E_{We} = 1$, and $\Gamma = 4899$ [5]. We can see that two dominant unstable modes emerge in the diagram of the spectrum where the phase speed of the shear mode is lower than that of the surface mode. However, the temporal growth rate of the shear mode is higher than that of the surface mode for the given parameter values. Hence, the surface mode propagates faster than the shear mode, but it is linearly less unstable than the shear mode. On the other hand, Fig. 2(c) illustrates the shapes of the absolute values of the normalized eigenfunctions corresponding to the surface mode and the shear mode, respectively. Although both the eigenfunctions increase monotonically from a zero value at the inclined plane to a maximum value at the fluid surface, they have distinct shapes from each other. More specifically, the amplitude of the velocity perturbation for the surface mode has a large variation in the vicinity of the fluid surface, but the amplitude of the velocity perturbation for the shear mode has a large variation close to the rigid wall rather than the fluid surface [see Fig. 2(c)]. Before exploring the effect of the electric field on the three-dimensional flow configuration, we first reproduce the results for the two-dimensional electrified flow configuration [30], which, in fact, justify the accuracy of the current numerical code. As a consequence, we set the spanwise wave number $\beta = 0$ in the numerical computation. Figure 3(a) illustrates the variation of the neutral curve for the surface mode as the electric Weber number changes when $\theta = 45^\circ$, $\beta = 0$, and Ca $= 2$ [30]. It is found that all the neutral curves for the surface mode intersect the Re axis at the known value $(5/4)\cot\theta$ in the limit $k \to 0$ or, equivalently, in the limit $\alpha \to 0$ ($k = \alpha$ as $\beta = 0$) for different values of the electric Weber number E_{We}. This result implies that the onset of instability for the surface mode corresponding to the electrified falling film remains the same even though the electric Weber number alters, which is fully consistent with the analytical result given by Blyth [30] in the long-wave regime, where it was shown that the onset of the surface mode instability is independent of the electric Weber number. Actually, the electric Weber number appears in the normal stress boundary condition (40) in the order $O(k^3)$ term. For this reason, it has no contribution to the critical Reynolds number for the onset of the surface mode instability because the critical Reynolds number is calculated from the first-order $O(k)$ equations in long-wave expansion. However, the unstable region induced by the surface mode magnifies gradually with the rising values of the electric Weber number E_{We} in the finite streamwise wave number regime. More specifically, some portion of the neutral curve is tweaked towards the α axis in the finite streamwise wave number regime with increasing E_{We}, and, suddenly, the neutral curve is divided into two distinct unstable zones bounded by two separate neutral curves at $E_{We} = 1.005$, as demonstrated by Blyth [30]. In fact, the new unstable zone emerges in the finite streamwise wave number regime and the associated neutral curve intersects the α axis rather than the Re axis, which results in an unstable range of finite streamwise wave number α, where the inertialess flow (Re $= 0$) is unstable. It is evident that the inertialess instability begins in the finite streamwise wave number regime before initiating the inertia-dependent long-wave surface mode instability. If the electric Weber number is further increased, these two neutral curves generate two new branches at $E_{We} = 1.03$ [see Fig. 3(b)]. In this case, we have one unstable zone rather than two. It should be noted that as E_{We} increases, the unstable range of the streamwise wave number for the inertialess instability expands. If we continue to increase the magnitude of E_{We}, the lower branch of the neutral curve moves in a downward direction, while the upper branch moves in an upward direction. This fact is followed by an increase in the unstable range of the streamwise wave number for the inertialess instability as the electric Weber number increases. In other words, the stable region for the surface mode decays successively with increasing E_{We}. From the above results, one can opine that the electric field or, equivalently, the electric Weber number has a destabilizing effect on the primary instability induced by the surface mode. Actually, the base flow solution for pressure [see Eq. (17)] shows that the impact

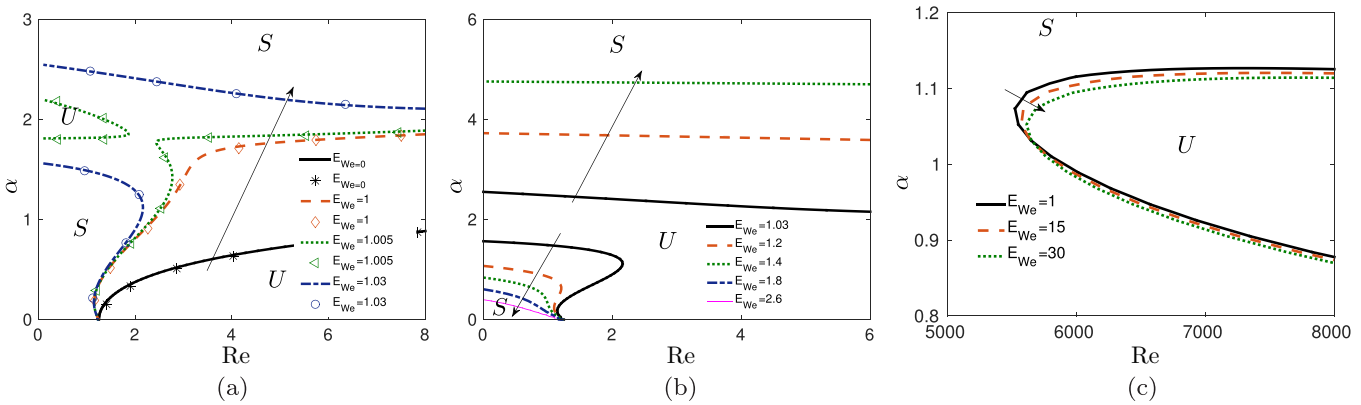

FIG. 3. (a) Variation of the neutral curve for the surface mode in the (Re, α) plane when $\theta = 45^\circ$, $\beta = 0$, and Ca = 2 [30]. Different point symbols are the results of Blyth [30]. (b) Variation of the upper and lower branches of the neutral curve for the surface mode as the electric Weber number E_{We} changes. The arrow points out the direction of the increasing unstable region with increasing E_{We}. (c) Variation of the neutral curve for the shear mode in the (Re, α) plane when $\theta = 1^\circ$, $\beta = 0$, and $\Gamma = 4899$ [5]. The arrow points out the direction of the decreasing unstable region with increasing E_{We}. "U" and "S" indicate unstable and stable zones.

of basic hydrostatic pressure responsible for the stabilizing effect reduces as the magnitude of the uniform electric field rises. As a result, less fluid moves towards the trough from the crest of the deformed fluid surface due to the basic hydrostatic pressure in comparison with the case of no electric field [47], and this causes a destabilizing effect on the primary instability. Moreover, all the results shown in Figs. 3(a) and 3(b) are identical to those of Blyth [30] when the spanwise wave number is set to zero ($\beta = 0$). On the other hand, Fig. 3(c) displays the variation of the neutral curve for the shear mode in the (Re, α) plane as the electric Weber number rises when $\theta = 1^\circ$, $\beta = 0$, and $\Gamma = 4899$ [5]. In this case, the interesting result is that the critical Reynolds number for the onset of the shear mode instability is dependent on the electric Weber number because the critical Reynolds number increases with the increasing value of the electric Weber number. This fact is opposed to the result of the surface mode instability, where the critical Reynolds number after which the instability initiates is independent of the electric Weber number. Obviously, there appears only one unstable region in the (Re, α) plane for the shear mode, which attenuates slightly with an increase in the value of the electric Weber number. Therefore, the electric Weber number has a stabilizing influence on the shear mode instability when $\theta = 1^\circ$, $\beta = 0$, and $\Gamma = 4899$. This result is in contrast to the result of the surface mode instability, where the unstable region magnifies with the increasing value of the electric Weber number.

A. Effect of the spanwise wave number on the surface mode and the shear mode for three-dimensional disturbance

Now, if the spanwise wave number is included in the numerical simulation ($\beta \neq 0$), the unstable region created by the surface mode changes dramatically. To exhibit this result, the numerical simulation is carried out for two different values of the electric Weber number E_{We}. If we set $E_{We} = 1.005$, the unstable region that intersects the Re axis shrinks significantly with increasing spanwise wave number β [see Fig. 4(a)]. The interesting result is that the onset of the surface mode instability gradually shifts towards the finite streamwise wave number regime, as was pointed out by Samanta [44] for a three-dimensional fluid flowing over a compliant substrate. Furthermore, the unstable region that intersects the α axis shrinks slightly with increasing β. This result implies that the spanwise wave number has a stabilizing effect on the surface mode instability. Furthermore, as the spanwise wave number rises, we observe that the long-wave surface mode instability disappears because the neutral curve for the surface mode no longer intersects the Re axis in the limit $\alpha \to 0$ [see Fig. 4(a)]. More specifically, this is the situation when both the streamwise and spanwise wave numbers are finite. In addition, we can predict that the unstable range of the streamwise wave number α for the inertialess instability will decay if the spanwise wave number β is increased. Next, the numerical simulation is accomplished at $E_{We} = 1.03$. In this case, the unstable region bounded by two branches of the neutral curve attenuates as the spanwise wave number rises [see Fig. 4(b)]. This result also supports the stabilizing influence of the spanwise wave number on the surface mode instability. In order to compare with the study of the nonelectrified falling film, the numerical experiment is further repeated at $E_{We} = 0$. Clearly, the neutral curve for the inertialess instability, which intersected the α axis in the electrified case, vanishes at $E_{We} = 0$ [see Fig. 4(c)]. In other words, we have not found any range of the streamwise wave number where the inertialess instability occurs. There exists only one neutral curve for the surface mode, which touches the Re axis when $\beta = 0.005$. As soon as the spanwise wave number increases, the neutral curve for the surface mode no longer touches the Re axis but forms a tonguelike shape, and the associated unstable region decreases, as was noticed for the electrified case. A similar stabilizing effect of the spanwise wave number on the surface mode instability was reported by Chang *et al.* [7] for the nonelectrified falling film by using the governing equations based on the boundary layer approximation. On the other hand, Fig. 4(d) displays the variation of the neutral curve for the shear mode as the spanwise wave number rises when $E_{We} = 1$. It should be noted that the spanwise wave number exhibits a similar behavior in the shear mode as was observed for the surface mode. In particular, the unstable region induced by

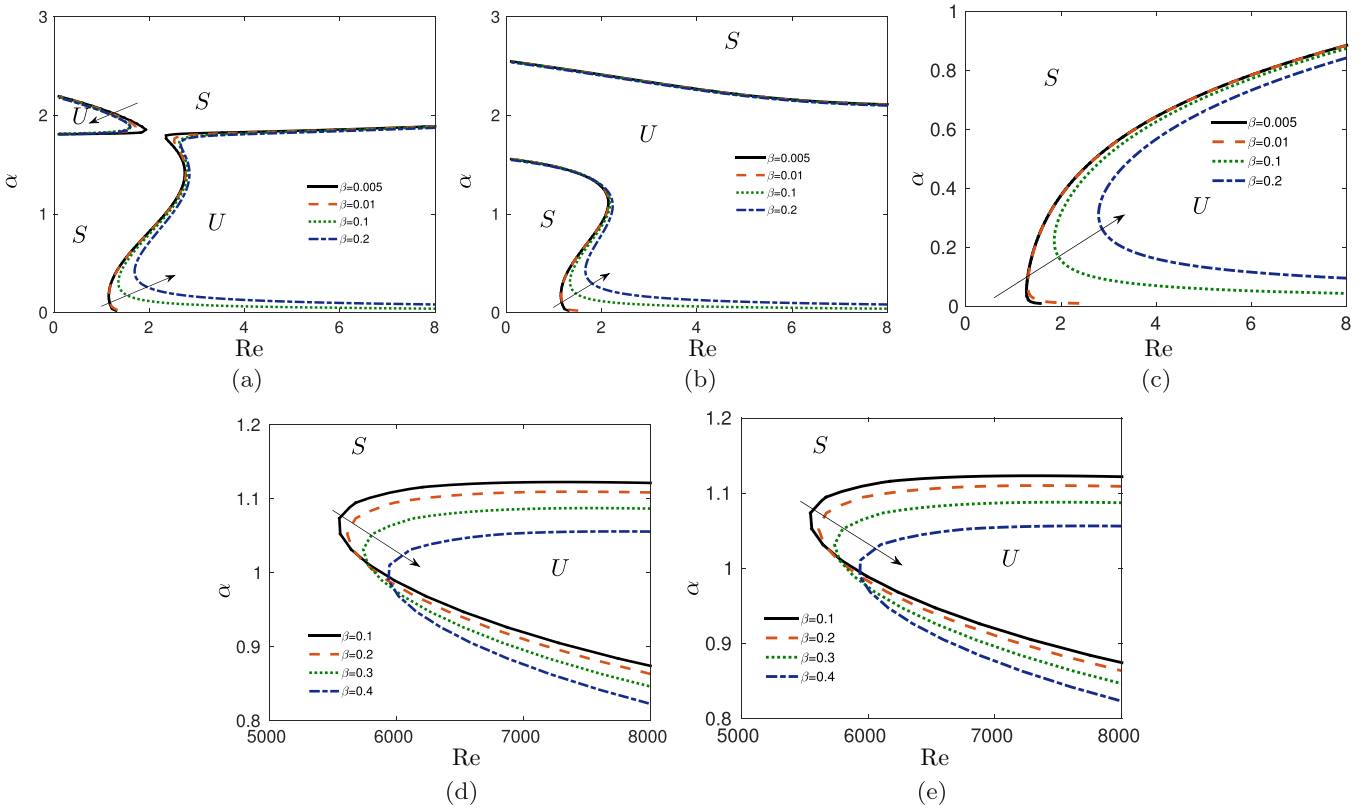

FIG. 4. Variation of the neutral curve for the surface mode in the (Re, α) plane for different values of the spanwise wave number β when $\theta = 45^\circ$ and Ca $= 2$. (a) $E_{We} = 1.005$, (b) $E_{We} = 1.03$, and (c) $E_{We} = 0$. Variation of the neutral curve for the shear mode in the (Re, α) plane for different values of the spanwise wave number β when $\theta = 1^\circ$ and $\Gamma = 4899$. (d) $E_{We} = 1$ and (e) $E_{We} = 0$. The arrow points out the direction of the decreasing unstable region with increasing β. "U" and "S" indicate unstable and stable zones.

the shear mode decreases successively with an increase in the value of β, which is followed by the successive increment of the critical Reynolds number for the onset of the shear mode instability. Hence, the spanwise wave number has a stabilizing influence on the shear mode instability. To compare with the results of the nonelectrified falling film, we further produce the results for the shear mode when $E_{We} = 0$. In this case, the neutral curve for the shear mode varies exactly in a similar fashion as was perceived in the electrified case [see Figs. 4(d) and 4(e)]. However, the onset of the shear mode instability for the nonelectrified falling film is slightly lower than that of the electrified falling film because the electric field has a stabilizing influence on the shear mode instability. The above results, computed based on the modal stability analysis, are completely in favor of the statement of Squire's theorem that the two-dimensional infinitesimal disturbance is linearly more unstable than the three-dimensional ones [48]. The analytical derivation of Squire's theorem for the electrified falling film is further discussed in Appendix A.

B. Effect of the electric field on the surface mode and the shear mode for three-dimensional disturbance

In order to explore the influence of the electric field on the surface mode in the wave number plane, we choose the following flow parameters: Re $= 2$, Ca $= 2$, and $\theta = 45^\circ$, as was suggested by Blyth [30] for the two-dimensional electrified falling film. Figures 5(a)–5(d) demonstrate the shape of the neutral curve for the surface mode in the (α, β) plane as the electric Weber number E_{We} alters. We can see that there appears only one unstable region I at $E_{We} = 1$, where the associated neutral curve intersects the α axis and passes through the origin [see Fig. 5(a)]. As soon as the electric Weber number is increased to $E_{We} = 1.005$, two additional unstable regions II and III emerge in the (α, β) plane [see Fig. 5(b)]. It should be noted that the neutral curve, which encloses the unstable region II, intersects the α axis but does not pass through the origin, while the neutral curve, which encloses the unstable region III, intersects the β axis and also does not pass through the origin. Moreover, the unstable region I slightly magnifies with increasing E_{We}. If the electric Weber number is further increased, we see that the unstable regions II and III are no longer separated from each other, but they merge at $E_{We} = 1.03$ and generate a new unstable region in the finite wave number regime [see Fig. 5(c)]. In this case, there are two branches of the neutral curve that enclose the new merged unstable region. Moreover, a stable region is created between the unstable region I and the new merged unstable region. If we continue to increase the magnitude of the electric Weber number, the lower branch of the merged unstable region coalesces with the unstable region I and, ultimately, they form a single unstable region which significantly enhances as the electric Weber number rises [see Fig. 5(d)]. The topology of the neutral curve for the surface mode is shown in the (α, E_{We}, β) plane [see Fig. 5(e)], which is fully consistent with the variation of the neutral curve displayed in

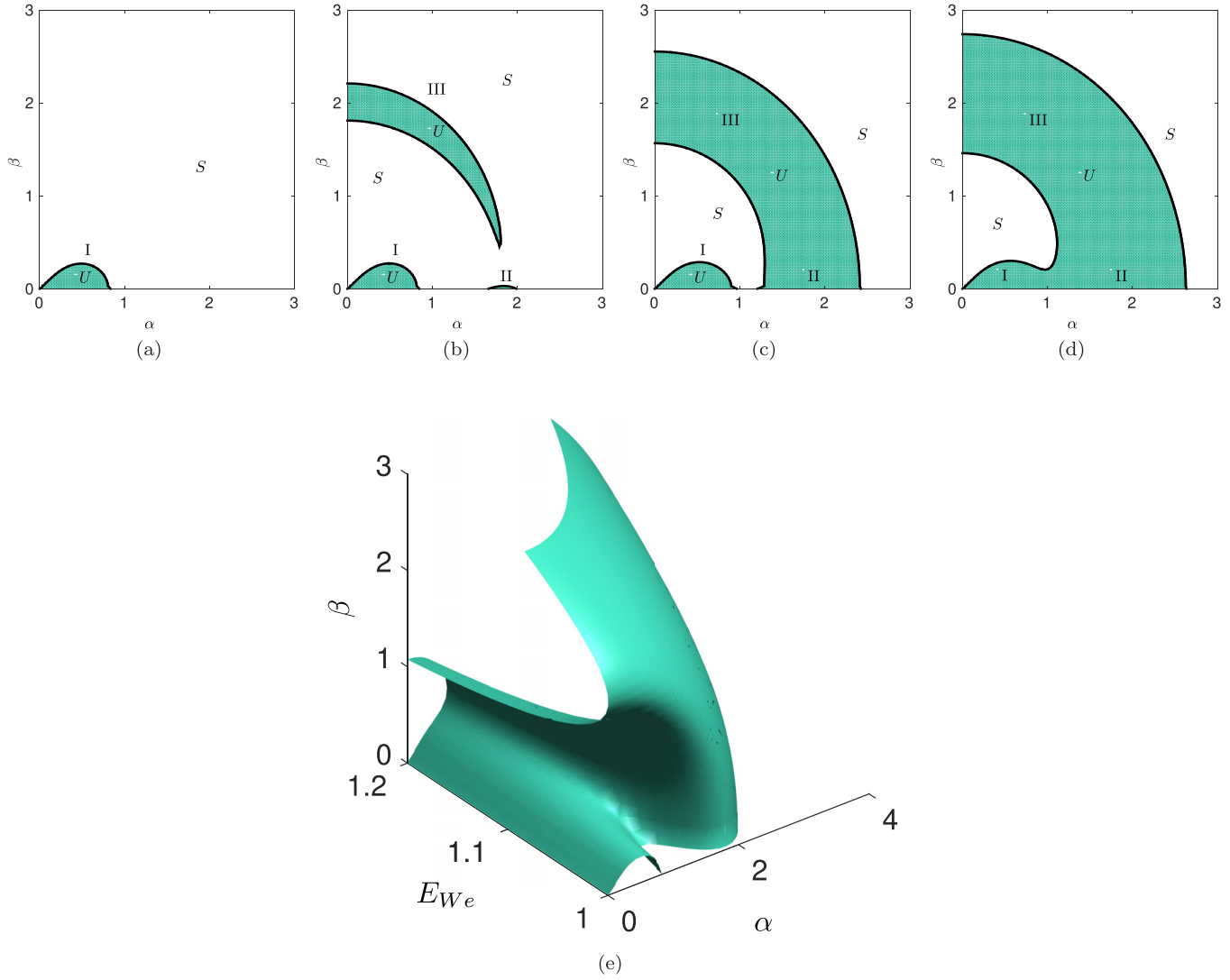

FIG. 5. Variation of the neutral curve for the surface mode in the (α, β) plane for different values of the electric Weber number E_{We} when $\theta = 45^\circ$, Ca $= 2$, and Re $= 2$. (a) $E_{We} = 1$, (b) $E_{We} = 1.005$, (c) $E_{We} = 1.03$, and (d) $E_{We} = 1.05$. (e) The isosurface plot of the neutral curve for the surface mode in the (α, E_{We}, β) plane. "U" and "S" indicate unstable and stable zones.

Figs. 5(a)–5(d). Figures 6(a)–6(d) illustrate the shape of the neutral curve for the shear mode in the wave number plane as the electric Weber number varies when $\theta = 1^\circ$, $\Gamma = 4899$, and Re $= 8000$ [5]. In this case, we see only one unstable region for the shear mode in the (α, β) plane for different values of the electric Weber number, where the associated neutral curve intersects the α axis, but does not pass through the origin. Furthermore, we can see that the unstable region becomes slightly smaller as the electric Weber number increases, which can also be figured out from the isosurface plot of the neutral curve in the (α, E_{We}, β) plane [see Fig. 6(e)]. Hence, the shear mode instability cannot be altered significantly by varying the electric Weber number when $\theta = 1^\circ$, $\Gamma = 4899$, and Re $= 8000$.

VI. NONMODAL STABILITY ANALYSIS

As discussed by Butler and Farrell [11], Trefethen *et al.* [12], Schmid and Henningson [13], Farrell [49], and Schmid [50], short-time or transient disturbance energy growth exists for the wall-bounded shear flows because the associated eigenvalue operator is non-normal for such flows. As a result, the critical Reynolds number for the onset of the shear mode instability cannot be accurately predicted by the traditional modal stability analysis. Recently, Olsson and Henningson [14] and Samanta [15,16] also demonstrated the existence of transient disturbance energy growth for the free surface flows. For this reason, we are also motivated to study the nonmodal stability analysis for an electrified falling film. The interesting fact of the nonmodal stability analysis is that the flow configuration may not be stable in the subcritical regime (Re $<$ Re$_c$) due to the occurrence of transient disturbance energy growth even though all eigenvalues lie in the stable lower-half plane ($\omega_i < 0$), where Re$_c$ is the critical Reynolds number for the onset of the shear mode instability. Therefore, one can make a wrong judgment regarding the stability or instability of a given flow configuration based on the traditional modal stability analysis. Hence, the study of nonmodal stability analysis is more relevant for characterizing a flow configuration if the associated eigenvalue operator is

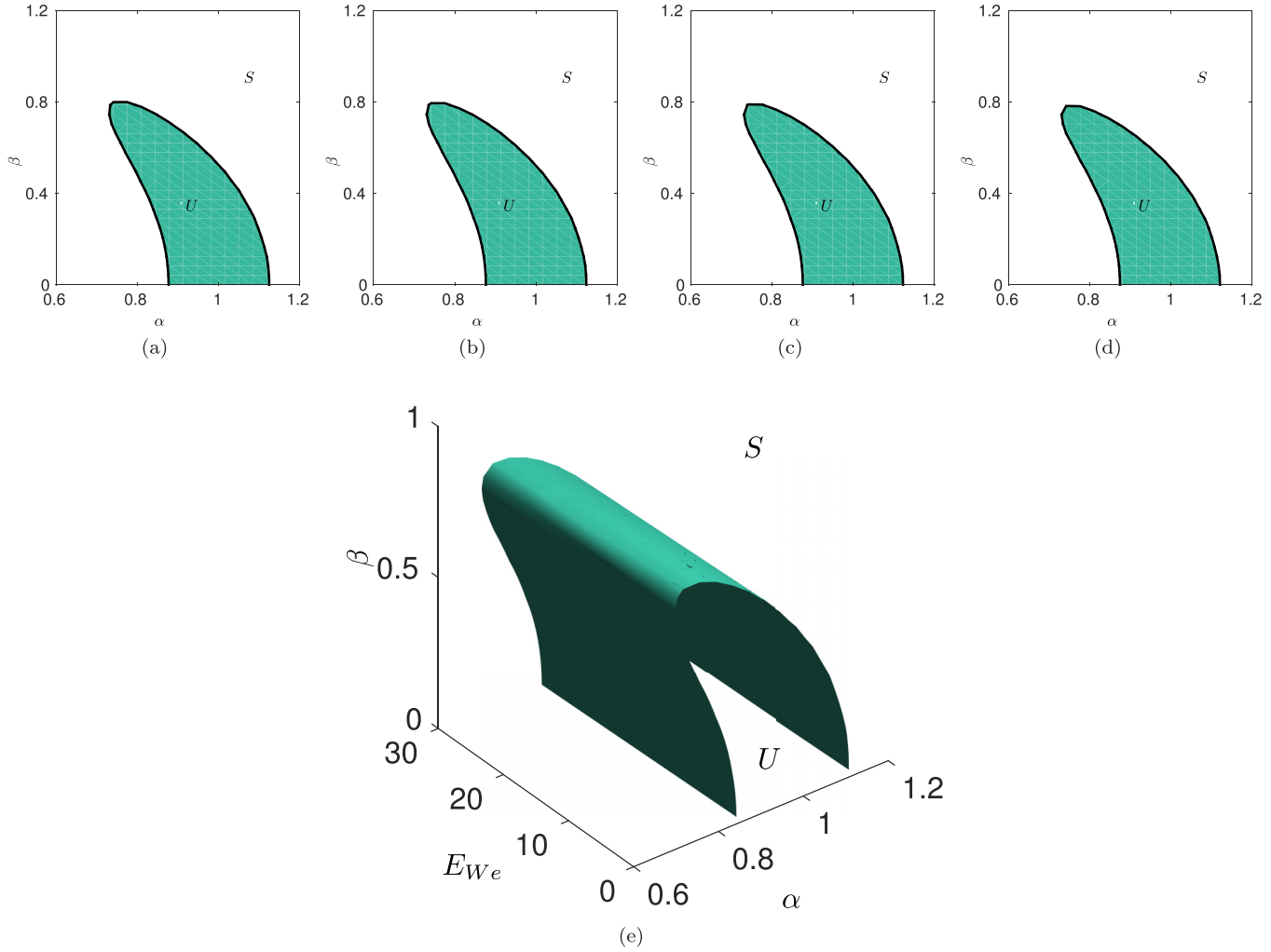

FIG. 6. Variation of the neutral curve for the shear mode in the (α, β) plane for different values of the electric Weber number E_{We} when $\theta = 1^\circ$, $\Gamma = 4899$, and $\mathrm{Re} = 8000$. (a) $E_{We} = 1$, (b) $E_{We} = 5$, (c) $E_{We} = 10$, and (d) $E_{We} = 15$. (e) The isosurface plot of the neutral curve for the shear mode in the (α, E_{We}, β) plane. "U" and "S" indicate stable and unstable zones.

non-normal. In the present flow configuration, the coupling terms in Eq. (42) make the eigenvalue operator non-normal because the evolutions of normal vorticity and fluid surface deformation depend on normal velocity [see Eq. (43)]. As a result, the superposition of eigenvectors becomes nonorthogonal and yields a short-time disturbance energy growth [13]. For instance, Fig. 7 displays the spectrum of the eigenvalue problem (45) obtained from the modal stability analysis when $\mathrm{Re} = 2000 < \mathrm{Re}_c$ [see, also, Fig. 4(d)]. We see that all eigenvalues lie in the stable lower-half plane ($\omega_i < 0$), which indicates a stable flow configuration for the given parameter values. But the numerical range [15,16,50] obtained from the nonmodal stability analysis enters the unstable upper-half plane ($\omega_i > 0$), which indicates the existence of short-time disturbance energy growth for an electrified falling film. How to compute the numerical range is discussed later in this section. Therefore, the nonmodal stability analysis is adequate for the electrified falling film. In particular, Fig. 7(a) depicts a symmetric shape of the spectrum with respect to Squire's branch (S branch) when $\alpha = 0$ and $\beta = 1$. Obviously, all eigenvalues in the S branch have a zero angular frequency ($\omega_r = 0$) in the absence of the streamwise wave number in the perturbation. Furthermore, all eigenvalues in the S branch are highly

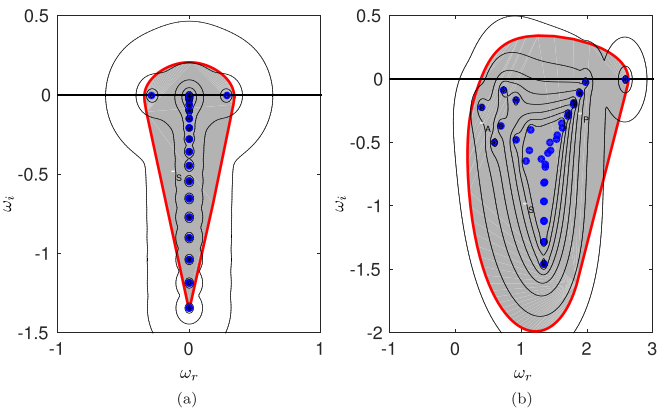

FIG. 7. Spectrum of the eigenvalue problem (45) specified by blue points, pseudospectra specified by thin solid lines, and numerical range specified by a thick solid line in the (ω_r, ω_i) plane when $\theta = 1^\circ$, $\Gamma = 4899$, $\mathrm{Re} = 2000$, and $E_{We} = 1$. (a) $\alpha = 0$ and $\beta = 1$. (b) $\alpha = 2$ and $\beta = 0.25$.

damped because $\omega_i < 0$. That is why the S branch is also referred to here as the Squire branch. However, if the streamwise wave number is incorporated in the perturbation ($\alpha \neq 0$), two new branches (A and P branches) along with the S branch appear in the diagram of the spectrum with different angular frequencies ($\omega_r \neq 0$) when $\alpha = 2$ and $\beta = 0.25$, which results in an asymmetric shape of the spectrum with respect to the S branch [see Fig. 7(b)]. In the nonmodal analysis, the energy norm is the physically important quantity for measuring the growth of the disturbance, which can be expressed as [14–16]

$$\mathcal{E}(\hat{q}) = \|\hat{q}\|_E^2 = \mathcal{E}_{\text{kin}} + \mathcal{E}_g + \mathcal{E}_\sigma + \mathcal{E}_{We}, \tag{47}$$

where

$$\mathcal{E}_{\text{kin}} = \frac{1}{2k^2}\int_0^1 \left(\left|\frac{\partial \hat{v}}{\partial y}\right|^2 + k^2|\hat{v}|^2 + |\hat{\Omega}|^2\right)dy,$$

$$\mathcal{E}_g = \frac{\cos\theta}{2\text{Fr}^2}|\hat{h}|^2,$$

$$\mathcal{E}_\sigma = \frac{k^2\text{We}}{2}|\hat{h}|^2,$$

$$\mathcal{E}_{We} = -\frac{kE_{We}}{\text{Re}}|\hat{h}|^2,$$

where $\mathcal{E}_{\text{kin}}$ represents the kinetic energy density norm per unit volume, which is the total kinetic energy of the perturbation after integration in a Fourier space, $\mathcal{E}_g$ represents the gravitational energy density norm per unit volume appearing due to the normal component of gravity, $\mathcal{E}_\sigma$ represents the surface energy density norm per unit volume appearing due to surface tension, and $\mathcal{E}_{We}$ represents the Maxwell energy density norm appearing due to the presence of the electric field. In fact, these three energy norms, $\mathcal{E}_g$, $\mathcal{E}_\sigma$, and $\mathcal{E}_{We}$, are absent from the energy norm for the wall-bounded shear flows because there is no deformed fluid surface. More specifically, these three energy density norms, $\mathcal{E}_g$, $\mathcal{E}_\sigma$, and $\mathcal{E}_{We}$, arise in the electrified falling film because the film surface is deformed due to perturbation, and thus the works done by the perturbation are required against the depthwise gravitational force, surface tension, and the electric field. Basically, these three energy norms are obtained by integrating the respective surface energies caused by the depthwise gravitational force, surface tension, and the electric field in a Fourier space. Now, for computing the disturbance energy norm $\mathcal{E}(\hat{q})$, we need the solution $\hat{q}(t)$ of the temporal matrix initial value problem (42), which can be deduced by using the initial condition $\hat{q}_0(t=0)$ as

$$\hat{q}(t) = \mathcal{C}\hat{q}_0, \tag{48}$$

where $\mathcal{C} = \exp[(\mathcal{B}^{-1}\mathcal{A})t] = \exp[\mathcal{H}t]$ $(\mathcal{H} = \mathcal{B}^{-1}\mathcal{A})$ is the linear temporal evolution operator acting on the initial perturbation $\hat{q}_0$ to evolve forward in time. Clearly, the behavior of solution $\hat{q}(t)$ with time depends on the variation of the linear temporal evolution operator $\exp[\mathcal{H}t]$. Hence, it is essential to figure out the behavior of the linear temporal evolution operator as time progresses. To do that, we compute the upper and lower bounds of $\exp[\mathcal{H}t]$ [13],

$$e^{\lambda_{\max}(\mathcal{H})t} \leqslant ||\exp[\mathcal{H}t]|| = ||\exp[\mathcal{S}\Lambda\mathcal{S}^{-1}t]|| \leqslant ||\mathcal{S}||||\mathcal{S}^{-1}||e^{\lambda_{\max}(\mathcal{H})t}, \tag{49}$$

where Λ is the diagonal matrix, $\lambda_{\max}(\mathcal{H})$ is the largest eigenvalue of $\mathcal{H}$, and $\text{Cond}(\mathcal{S}) = \|\mathcal{S}\|\|\mathcal{S}^{-1}\|(\geqslant 1)$ is the condition number of the matrix $\mathcal{S}$. The expression (49) implies that all times behavior of the linear temporal evolution operator is driven by the least stable eigenvalue $\lambda_{\max}(\mathcal{H})$ if $\text{Cond}(\mathcal{S}) = 1$, which is exactly the situation when the matrix operator $\mathcal{H}$ is normal. In this case, the study of eigenvalues is sufficient to characterize the stability or instability of a flow configuration at all times. However, if $\text{Cond}(\mathcal{S}) > 1$, the least stable eigenvalue $\lambda_{\max}(\mathcal{H})$ governs only the asymptotic or long-time behavior of the linear temporal evolution operator, which is exactly the situation for the non-normal matrix operator $\mathcal{H}$. In this case, we require investigation of both the eigenvalues and eigenvectors of the matrix operator $\mathcal{H}$. Therefore, the computation of the numerical range is more appropriate than the computation of eigenvalues for the non-normal matrix operator. The numerical range is defined as [51]

$$\left[\hat{p} \in \mathbb{C} : \hat{p} = \frac{\langle \mathcal{H}\hat{q}, \hat{q}\rangle}{\langle \hat{q}, \hat{q}\rangle} = \frac{\hat{q}^H\mathcal{H}\hat{q}}{\hat{q}^H\hat{q}}\right], \tag{50}$$

where the inner product is defined as $\langle \hat{q}, \hat{q}\rangle = \hat{q}^H\hat{q}$. Here, $\mathbb{C}$ is the set of complex numbers. The superscript "H" denotes the conjugate transpose. Based on the above definition (50), the numerical range is computed for the set of flow parameters $\theta = 1^\circ$, $\Gamma = 4899$, $\text{Re} = 2000$, and $E_{We} = 1$, and illustrated in Fig. 7. We can see that the numerical range specified by the thick solid line enters the upper-half plane ($\omega_i > 0$), which ensures the appearance of transient disturbance energy growth. Following the studies of Reddy and Henningson [52] and Barkley *et al.* [53], we define the optimal energy amplification function $\mathcal{G}(t)$ as

$$\mathcal{G}(t) = \max_{\hat{q}_0\neq 0}\frac{\mathcal{E}(\hat{q})}{\mathcal{E}(\hat{q}_0)} = \max_{\hat{q}_0\neq 0}\frac{\|\hat{q}\|_E^2}{\|\hat{q}_0\|_E^2} = \max_{\hat{q}_0\neq 0}\frac{\langle \mathcal{C}\hat{q}_0, \mathcal{C}\hat{q}_0\rangle}{\langle \hat{q}_0, \hat{q}_0\rangle} = \max_{\hat{q}_0\neq 0}\frac{\langle \hat{q}_0, \mathcal{C}^*\mathcal{C}\hat{q}_0\rangle}{\langle \hat{q}_0, \hat{q}_0\rangle} = \lambda_{\max}(\mathcal{C}^*\mathcal{C}), \tag{51}$$

where $\lambda_{\max}(\mathcal{C}^*\mathcal{C})$ is the largest eigenvalue of $\mathcal{C}^*\mathcal{C}$ and $\mathcal{C}^*$ is the adjoint operator of $\mathcal{C}$, while the energy norm is defined as $\|\hat{q}\|_E^2 = \langle \hat{q}, \hat{q}\rangle$. It should be noted that the optimal energy amplification function $\mathcal{G}(t)$ is maximized over all initial conditions $\hat{q}_0$. Indeed, Eq. (51) implies that the computation of the optimal energy amplification function $\mathcal{G}(t)$ is equivalent to the computation of the largest eigenvalue of the matrix $\mathcal{C}^*\mathcal{C}$ or, equivalently, the computation of the largest singular value of the matrix $\mathcal{C}$. Using the definition of singular-value decomposition, one can write

$$\mathcal{C}\mathcal{U} = \mathcal{V}\Sigma, \tag{52}$$

where $\mathcal{U}$ and $\mathcal{V}$ are the unitary matrices, and Σ is the diagonal matrix whose elements are the singular values of the matrix $\mathcal{C}$. Suppose that σ_0 is the largest singular value of the matrix $\mathcal{C}$, and u_0 and v_0 are the associated left and right singular vectors. Then one can write

$$\mathcal{C}u_0 = \sigma_0 v_0. \tag{53}$$

Equation (53) indicates that the temporal evolution operator $\mathcal{C}$ modifies the initial state of perturbation $\hat{q}_0 = u_0$ to its final state of perturbation $\hat{q} = v_0$ at time t accompanied by an optimal energy amplification $\mathcal{G}(t) = \sigma_0$. In Fig. 8, we have

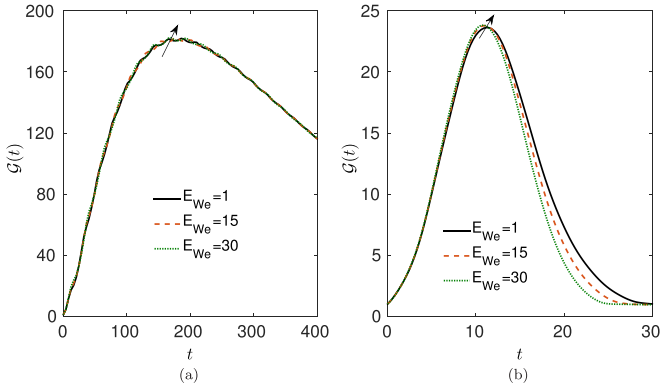

FIG. 8. Variation of the optimal energy amplification function $\mathcal{G}(t)$ with time t for different values of the electric Weber number E_{We} when $\theta = 1^\circ$, $\Gamma = 4899$, and $\mathrm{Re} = 2000$. (a) $\alpha = 0$ and $\beta = 1$. (b) $\alpha = 2$ and $\beta = 0.25$.

depicted the variation of the optimal energy amplification function $\mathcal{G}(t)$ with time t as the electric Weber number rises. As predicted before, the transient disturbance energy growth appears and intensifies slightly with an increase in the value of the electric Weber number. In the first case, we assume that the disturbance is independent of the streamwise wave number ($\alpha = 0$, $\beta = 1$), while in the second case, we assume that the disturbance contains both the streamwise and spanwise wave numbers ($\alpha = 2$ and $\beta = 0.25$). Obviously, the transient disturbance energy growth becomes higher in comparison with the disturbance, which includes both the streamwise and spanwise wave numbers. Following the studies of Olsson and Henningson [14] and Samanta [15,16], we also compute the contours of $\mathcal{G}^T_{\max}$ in the (α, β) plane when the Reynolds number changes. It should be useful to point out that $\mathcal{G}^T_{\max} = \max_{t>0}\mathcal{G}(t)$, which is maximized over time. In Fig. 9(a), we see that the transient disturbance energy growth occupies the entire wave number plane when $\mathrm{Re} = 500$, where the shaded region represents the zone for the surface mode instability,

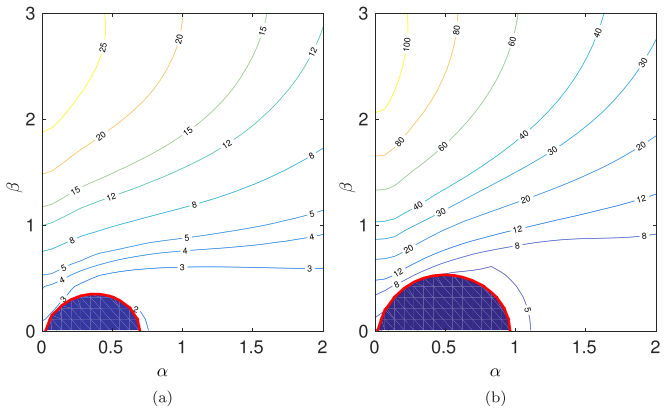

FIG. 9. Contours of the maximum energy amplification function over time, $\mathcal{G}^T_{\max}$, in the (α, β) plane for different values of the Reynolds number Re when $\theta = 1^\circ$, $\Gamma = 4899$, and $E_{We} = 1$. (a) $\mathrm{Re} = 500$. (b) $\mathrm{Re} = 1000$. The shaded region represents the unstable zone for the surface mode computed from the modal stability analysis.

which is computed by using the modal stability analysis. As a result, the infinitesimal disturbance will grow exponentially with time due to the surface mode instability if the streamwise and spanwise wave numbers are selected from this shaded zone for the given infinitesimal disturbance. By contrast, in the region of transient disturbance energy growth, the disturbance grows monotonically up to a certain value of time, where the transient disturbance energy growth reaches its maximum value, and then it decays as time progresses (see Fig. 8). Now, if the Reynolds number is increased and fixed at $\mathrm{Re} = 1000$, the shaded region for the surface mode instability magnifies [see Fig. 9(b)]. From the values on the isolines, we see that $\mathcal{G}^T_{\max}$ enhances with increasing Re, but gradually attenuates as the isoline approaches close to the shaded zone. This result is also in favor of the result shown in Fig. 8 because the transient disturbance energy growth decays at large time. Furthermore, the maximum value of the transient disturbance energy growth emerges in the vicinity of the spanwise wave number axis rather than the streamwise wave number axis, which is also consistent with the results demonstrated in Fig. 8.

Pseudoresonance phenomenon

Now, we shall examine the behavior of the response subjected to an external harmonic force applied on the electrified flow configuration. Consequently, we recast the initial value problem (42) in the following form by adding an additional external forcing term in the right-hand side of Eq. (42):

$$\partial_t \hat{q} = \mathcal{H}\hat{q} + \hat{f}e^{i\lambda t}, \tag{54}$$

where $\hat{f}$ and λ are the amplitude and frequency of the external harmonic force, respectively, and $\mathcal{H} = \mathcal{B}^{-1}\mathcal{A}$. Then, the amplitude of the particular solution of Eq. (54) can be expressed as

$$\hat{q} = (i\lambda\mathcal{I} - \mathcal{H})^{-1}\hat{f}, \tag{55}$$

where $\mathcal{I}$ is the identity matrix. As discussed by Trefethen *et al.* [12] and Schmid [54], the maximum response of the flow configuration can be determined by the ratio of two energy norms,

$$\mathcal{R}(\lambda) = \max_{\hat{f}} \frac{\|\hat{q}\|_E}{\|\hat{f}\|_E} = \|(i\lambda\mathcal{I} - \mathcal{H})^{-1}\|_E = \|[\mathcal{S}(i\lambda - \Lambda)^{-1}\mathcal{S}^{-1}]\|_E, \tag{56}$$

where Λ is the diagonal matrix, and $\mathcal{R}(\lambda)$ is also called the resolvent norm, which is maximized over all permissible initial forcing amplitudes $\hat{f}$. Actually, the resolvent norm operates on the initial forcing amplitude $\hat{f}$ with frequency λ and converts it to the final response [see Eq. (55)]. For a wall-bounded shear flow, Trefethen *et al.* [12] and Schmid [54] performed the resolvent analysis and showed that the pseudoresonance phenomenon occurs for the non-normal matrix operator, where the amplitude of the response subjected to an external harmonic force is very large even though the forcing frequency λ is different from the eigenvalue of the matrix operator $\mathcal{H}$. Such a pseudoresonance scenario is demonstrated in Fig. 10, which corresponds to the electrified falling film for two different sets of streamwise and spanwise wave numbers.

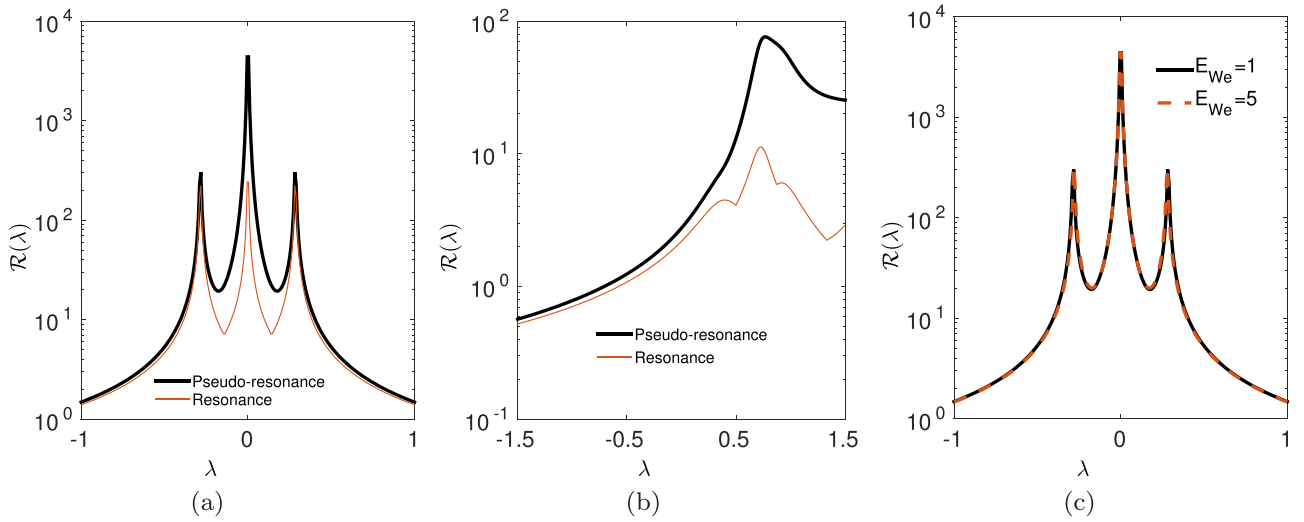

FIG. 10. Variation of the resolvent norm $\mathcal{R}(\lambda)$ as a function of forcing frequency λ when $E_{We} = 1$. (a) $\alpha = 0$ and $\beta = 1$. (b) $\alpha = 2$ and $\beta = 0.25$. Thick and thin lines represent the results for the pseudoresonance and resonance phenomena, respectively. (c) Variation of the resolvent norm $\mathcal{R}(\lambda)$ as a function of forcing frequency λ when the electric Weber number E_{We} changes. Solid and dashed lines represent the results for $E_{We} = 1$ and $E_{We} = 5$, respectively. The other flow parameter values are $\theta = 1^\circ$, $\Gamma = 4899$, and $\mathrm{Re} = 2000$.

In Figs. 10(a) and 10(b), the results for the pseudoresonance event are specified by the thick solid lines. In both cases, the resolvent norm displays strong peaks in the response curve. However, if the streamwise wave number is included in the disturbance, the maximum value of the pseudoresonance peak decreases significantly in comparison with the disturbance without the streamwise wave number. This fact is fully consistent with the results of transient disturbance energy growth shown in Fig. 8. Furthermore, the response curve corresponding to the resonance event exhibits a lower peak than that of the pseudoresonance event. In Figs. 10(a) and 10(b), the results for the resonance event are specified by the thin solid lines, which are computed numerically by using the norm $\|(i\lambda - \Lambda)^{-1}\|$. Figure 10(c) reveals that the electric field has no discernible impact on the pseudoresonance phenomenon.

VII. DISCUSSION AND CONCLUSIONS

The present study focuses on the modal and nonmodal stability analyses of an incompressible gravity-driven three-dimensional viscous fluid flowing down an inclined plane, where a uniform electric field is applied in the normal direction to the inclined plane at infinity. To explore the modal and nonmodal stability analyses, we develop the time evolution equations for normal velocity, normal vorticity, and fluid surface deformation, respectively. The Chebyshev spectral collocation method is implemented to solve the time evolution equations numerically. The modal stability analysis identifies two dominant modes, the so-called surface mode and the shear mode. For the two-dimensional disturbance ($\beta = 0$), the neutral curve varies drastically as the electric Weber number rises. For instance, the single unstable region bounded by the neutral curve is suddenly divided into two distinct unstable zones bounded by two distinct neutral curves at $E_{We} = 1.005$, as revealed by Blyth [30]. In particular, the new unstable zone appears in the finite streamwise wave number regime, and the associated neutral curve intersects the α axis instead of the Re axis, which causes an unstable range of the finite streamwise wave number where the electrified falling film experiences inertialess instability. Moreover, this unstable range of the streamwise wave number for the inertialess instability magnifies as the electric Weber number increases. For the three-dimensional disturbance, the results computed from the modal stability analysis demonstrate that there exist three unstable regions for the surface mode in the wave number plane when the electric Weber number is fixed at a low value. However, these unstable regions coalesce as soon as the electric Weber number is increased. The merged unstable region becomes larger with an increase in the value of the electric Weber number. By contrast, only one unstable region is found for the shear mode in the wave number plane, which depletes slightly as the electric Weber number rises. Furthermore, the streamwise wave number exhibits a stabilizing impact on both the surface and shear modes, which is consistent with the statement of Squire's theorem, where the three-dimensional infinitesimal disturbances are linearly less unstable than the two-dimensional ones. In addition, we see that the long-wave surface mode instability no longer exists, but shifts towards the finite wavelength regime as the spanwise wave number rises. On the other hand, from the results of the nonmodal stability analysis, we predict that the transient disturbance energy growth exists for the electrified falling film, and it becomes stronger for the spanwise disturbance than the disturbance that contains both the streamwise and spanwise wave numbers. Furthermore, its maximum value arises in the vicinity of the spanwise wave number axis instead of the streamwise wave number axis. However, we have not found a significant effect of the electric Weber number on the transient disturbance energy growth. The pseudoresonance event occurs when an external harmonic force is imposed on the given flow configuration. Again, the peak of the response curve for the spanwise disturbance is larger than that of the disturbance, which includes both the streamwise and spanwise wave numbers.

ACKNOWLEDGMENTS

The author would like to thank the reviewers for their constructive comments and suggestions on improving the manuscript. The author also acknowledges the support of the Science and Engineering Research Board (File No. MTR/2019/000019), Government of India.

APPENDIX A: SQUIRE'S THEOREM FOR THE ELECTRIFIED FALLING FILM

In order to develop an equivalent set of two-dimensional perturbation equations from the set of three-dimensional perturbation equations (19)–(29) for the electrified falling film, we shall propose some transformations as suggested by Blyth [30], Drazin and Reid [48], and Squire [55]. First, using the normal mode solution, we express the three-dimensional perturbation equations (19)–(29) in the following forms:

$$i\alpha\hat{u} + \partial_y\hat{v} + i\beta\hat{w} = 0, \tag{A1}$$

$$i\alpha(U-c)\hat{u} + \partial_y U\hat{v} + i\alpha\hat{p} - [\partial_{yy} - (\alpha^2+\beta^2)]\hat{u}/\mathrm{Re} = 0, \tag{A2}$$

$$i\alpha(U-c)\hat{v} + \partial_y\hat{p} - [\partial_{yy} - (\alpha^2+\beta^2)]\hat{v}/\mathrm{Re} = 0, \tag{A3}$$

$$i\alpha(U-c)\hat{w} + i\beta\hat{p} - [\partial_{yy} - (\alpha^2+\beta^2)]\hat{w}/\mathrm{Re} = 0, \tag{A4}$$

$$[\partial_{yy} - (\alpha^2+\beta^2)]\hat{\phi} = 0, \tag{A5}$$

$$\hat{u} = 0,\ \hat{v} = 0,\ \hat{w} = 0 \text{ at } y = 0, \tag{A6}$$

$$\partial_y\hat{u} + i\alpha\hat{v} + \hat{h}\partial_{yy}U = 0 \text{ at } y = 1, \tag{A7}$$

$$\partial_y\hat{w} + i\beta\hat{v} = 0 \text{ at } y = 1, \tag{A8}$$

$$\hat{\phi} - \hat{h} = 0 \text{ at } y = 1, \tag{A9}$$

$$-\hat{p} + (2/\mathrm{Re})\partial_y\hat{v} + (2E_{We}/\mathrm{Re})\partial_y\hat{\phi} + \mathrm{We}(\alpha^2+\beta^2)\hat{h} + (\cos\theta/\mathrm{Fr}^2)\hat{h} = 0 \text{ at } y = 1, \tag{A10}$$

$$i\alpha(U-c)\hat{h} = \hat{v} \text{ at } y = 1. \tag{A11}$$

$$\hat{\phi} = 0,\ \partial_y\hat{\phi} = 0 \text{ at } y \to \infty. \tag{A12}$$

Now, the following forms of the extended Squire's transformations [30,48] are used: $\alpha\hat{u} + \beta\hat{w} = \tilde{k}\tilde{u}$, $\hat{v} = \tilde{v}$, $\tilde{k}\hat{p} = \alpha\tilde{p}$, $\tilde{k} = \sqrt{\alpha^2+\beta^2}$, $c = \tilde{c}$, $\alpha\mathrm{Re} = \tilde{k}\tilde{\mathrm{Re}}$, $\alpha\hat{\phi} = \tilde{k}\tilde{\phi}$, $\tilde{k}^2\mathrm{We} = \alpha^2\tilde{\mathrm{We}}$, $\alpha^2\mathrm{Fr}^2 = \tilde{k}^2\tilde{\mathrm{Fr}}^2$, $\tilde{k}E_{We} = \alpha\tilde{E}_{We}$, and $\alpha\hat{h} = \tilde{k}\tilde{h}$. Using the above transformations, we can obtain a similar set of perturbation equations for the two-dimensional disturbance with a normal mode solution ($\propto \exp[i\tilde{k}(x-\tilde{c}t)]$),

$$i\tilde{k}\tilde{u} + \partial_y\tilde{v} = 0, \tag{A13}$$

$$i\tilde{k}(U-\tilde{c})\tilde{u} + \partial_y U\tilde{v} + i\tilde{k}\tilde{p} - (\partial_{yy} - \tilde{k}^2)\tilde{u}/\tilde{\mathrm{Re}} = 0, \tag{A14}$$

$$i\tilde{k}(U-\tilde{c})\tilde{v} + \partial_y\tilde{p} + (\partial_{yy} - \tilde{k}^2)\tilde{v}/\tilde{\mathrm{Re}} = 0, \tag{A15}$$

$$[\partial_{yy} - \tilde{k}^2]\tilde{\phi} = 0, \tag{A16}$$

$$\tilde{u} = 0,\ \tilde{v} = 0 \text{ at } y = 0, \tag{A17}$$

$$\partial_y\tilde{u} + i\tilde{k}\tilde{v} + \tilde{h}\partial_{yy}U = 0 \text{ at } y = 1, \tag{A18}$$

$$\tilde{\phi} - \tilde{h} = 0 \text{ at } y = 1, \tag{A19}$$

$$-\tilde{p} + (2/\tilde{\mathrm{Re}})\partial_y\tilde{v} + (2\tilde{E}_{We}/\tilde{\mathrm{Re}})\partial_y\tilde{\phi} + \tilde{\mathrm{We}}\,\tilde{k}^2\tilde{h} + (\cos\theta/\tilde{\mathrm{Fr}}^2)\tilde{h} = 0 \text{ at } y = 1, \tag{A20}$$

$$i\tilde{k}(U-\tilde{c})\tilde{h} = \tilde{v} \text{ at } y = 1, \tag{A21}$$

$$\tilde{\phi} = 0,\ \partial_y\tilde{\phi} = 0 \text{ at } y \to \infty, \tag{A22}$$

where $\tilde{k}$ is the wave number and $\tilde{c}$ is the wave speed of the two-dimensional infinitesimal disturbance. The other "tilde" quantities are the variables for the two-dimensional disturbed flows. Clearly, the Reynolds number Re for the three-dimensional disturbance is greater than the Reynolds number $\tilde{\mathrm{Re}}$ for the two-dimensional disturbance because $\mathrm{Re} = (\tilde{k}/\alpha)\tilde{\mathrm{Re}} > \tilde{\mathrm{Re}}$, where $\beta \neq 0$. Hence, the modal instability corresponding to the three-dimensional infinitesimal disturbance occurs at a higher Reynolds number than that of the two-dimensional infinitesimal disturbance. In other words, compared to three-dimensional disturbances, we can conclude that the two-dimensional infinitesimal disturbance is linearly more unstable.

APPENDIX B: CHEBYSHEV SPECTRAL COLLOCATION METHOD

In this method, we first expand the perturbation amplitude functions $\tilde{v}$ and $\tilde{\Omega}$ in a truncated series of the Chebyshev polynomials [56,57],

$$\tilde{v}(y) = \sum_{j=0}^{N} v_j T_j(y),\ \tilde{\Omega}(y) = \sum_{j=0}^{N} \Omega_j T_j(y), \tag{B1}$$

where v_j and Ω_j are unknown coefficients to be determined numerically. Since the Chebyshev polynomials of the first kind $T_j(y) = \cos(j\cos^{-1}y)$ are defined over the domain $[-1, 1]$, we shift the fluid layer domain [0,1] to $[-1, 1]$ using the transformation $y = (x+1)/2$, where $x \in [-1, 1]$. As a consequence, it is necessary to change the different order derivatives in the following way: $\partial_y \to 2\partial_y$, $\partial_{yy} \to 4\partial_{yy}$, ... Next, inserting Eq. (B1) into the eigenvalue problem (45), the Chebyshev functions are evaluated at the Gauss-Lobatto collocation points $x_i = \cos(\pi i/N)$, which are the extrema of the Chebyshev polynomials, where $i = 0, \ldots, N$.

[1] T. B. Benjamin, Wave formation in laminar flow down an inclined plane, J. Fluid Mech. **2**, 554 (1957).

[2] C. S. Yih, Stability of liquid flow down an inclined plane, Phys. Fluids **6**, 321 (1963).

[3] S. P. Lin, Instability of a liquid film flowing down an inclined plane, Phys. Fluids **10**, 308 (1967).

[4] G. J. De Bruin, Stability of a layer of liquid flowing down an inclined plane, J. Eng. Math. **8**, 259 (1974).

[5] R. W. Chin, F. H. Abernathy, and J. R. Bertschy, Gravity and shear wave stability of free surface flows. Part 1. Numerical calculations, J. Fluid Mech. **168**, 501 (1986).

[6] J. M. Floryan, S. H. Davis, and R. E. Kelly, Instabilities of a liquid film flowing down a slightly inclined plane, Phys. Fluids **30**, 983 (1987).

[7] H. C. Chang, E. A. Demekhin, and D. I. Kopelevich, Nonlinear evolution of waves on a vertically falling film, J. Fluid Mech. **250**, 433 (1993).

[8] H. C. Chang, Wave evolution on a falling film, Annu. Rev. Fluid Mech. **26**, 103 (1994).

[9] A. Oron, S. H. Davis, and S. G. Bankoff, Long scale evolution of thin films, Rev. Mod. Phys. **69**, 931 (1997).

[10] R. V. Craster and O. K. Matar, Dynamics and stability of thin liquid films, Rev. Mod. Phys. **81**, 1131 (2009).

[11] K. M. Butler and B. F. Farrell, Three-dimensional optimal perturbations in viscous shear flow, Phys. Fluids **4**, 1637 (1992).

[12] L. N. Trefethen, A. E. Trefethen, S. C. Reddy, and T. A. Driscoll, Hydrodynamic stability without eigenvalues, Science **261**, 578 (1993).

[13] P. J. Schmid and D. S. Henningson, *Stability and Transition in Shear Flows* (Springer, New York, 2001).

[14] P. J. Olsson and D. S. Henningson, Optimal disturbance growth in watertable flow, Stud. Appl. Math. **94**, 183 (1995).

[15] A. Samanta, Optimal disturbance growth in shear-imposed falling film, AIChE J. **66**, e16906 (2020).

[16] A. Samanta, Non-modal stability analysis in viscous fluid flows with slippery walls, Phys. Fluids **32**, 064105 (2020).

[17] H. Kim, S. G. Bankoff, and M. J. Miksis, The effect of an electrostatic field on film flow down an inclined plane, Phys. Fluids **4**, 2117 (1992).

[18] E. M. Griffing, S. G. Bankoff, M. J. Miksis, and R. A. Schluter, Electro-hydrodynamics of thin flowing films, J. Fluids Eng. **128**, 276 (2006).

[19] A. Gonzalez and A. Castellanos, Nonlinear electrodynamics waves on films falling down an inclined plane, Phys. Rev. E **53**, 3573 (1996).

[20] B. Tilley, P. Petropoulos, and D. Papageorgiou, Dynamics and rupture of planar electrified liquid sheets, Phys. Fluids **13**, 3547 (2001).

[21] D. Tseluiko and D. Papageorgiou, Wave evolution on electrified falling films, J. Fluid Mech. **556**, 361 (2006).

[22] J. R. Melcher and G. I. Taylor, Electrohydrodynamics: A review of the role of interfacial stresses, Annu. Rev. Fluid Mech. **1**, 111 (1969).

[23] D. T. Papageorgiou and P. G. Petropoulos, Generation of interfacial instabilities in charged electrified viscous liquid films, J. Eng. Math. **50**, 223 (2004).

[24] D. T. Papageorgiou, Film flows in the presence of electric fields, Annu. Rev. Fluid Mech. **51**, 155 (2019).

[25] C. Ruyer-Quil and P. Manneville, Improved modeling of flows down inclined planes, Eur. Phys. J. B **15**, 357 (2000).

[26] A. W. Wray, O. K. Matar, and D. T. Papageorgiou, Accurate low-order modeling of electrified falling films at moderate Reynolds number, Phys. Rev. Fluids **2**, 063701 (2017).

[27] W. Rohlfs, G. F. Dietze, H. D. Haustein, O. Yu. Tsvelodub, and R. Kneer, Experimental investigation into three-dimensional wavy liquid films under the influence of electrostatic forces, Expt. Fluids **53**, 1045 (2012).

[28] R. Verma, A. Sharma, K. Kargupta, and J. Bhaumik, Electric field induced instability and pattern formation in thin liquid films, Langmuir **21**, 3710 (2005).

[29] M. G. Blyth and C. Pozrikidis, Effect of surfactant on the stability of film flow down an inclined plane, J. Fluid Mech. **521**, 241 (2004).

[30] M. G. Blyth, Effect of an electric field on the stability of contaminated film flow down an inclined plane, J. Fluid Mech. **595**, 221 (2008).

[31] A. Samanta, Shear wave instability for electrified falling films, Phys. Rev. E **88**, 053002 (2013).

[32] A. Samanta, Spatiotemporal instability of an electrified falling film, Phys. Rev. E **93**, 013125 (2016).

[33] M. G. Blyth, D. Tseluiko, T.-S. Lin, and S. Kalliadasis, Two-dimensional pulse dynamics and the formation of bound states on electrified falling films, J. Fluid Mech. **855**, 210 (2018).

[34] D. A. Saville, Electrohydrodynamics: The Taylor-Melcher leaky dielectric model, Annu. Rev. Fluid Mech. **29**, 27 (1997).

[35] L. H. Gustavsson, Energy growth of three-dimensional disturbances in plane Poiseuille flow, J. Fluid Mech. **224**, 241 (1991).

[36] R. J. Tomlin, D. T. Papageorgiou, and G. A. Pavliotis, Three-dimensional wave evolution on electrified falling films, J. Fluid Mech. **822**, 54 (2017).

[37] K. Savettaseranee, D. T. Papageorgiou, P. G. Petropoulos, and B. S. Tilley, The effect of electric fields on the rupture of thin viscous films by van der waals forces, Phys. Fluids **15**, 641 (2003).

[38] A. Samanta, Effect of electric field on an oscillatory film flow, Phys. Fluids **31**, 034109 (2019).

[39] A. Samanta, Effect of electric field on the stability of an oscillatory contaminated film flow, Phys. Fluids **21**, 114101 (2009).

[40] D. A. Jackson, *Classical Electrodynamics* (Wiley, New York, 1963).

[41] R. Liu and Q. Liu, Instabilities and transient behaviors of a liquid film flowing down a porous inclined plane, Phys. Fluids **22**, 074101 (2010).

[42] F. A. Bhat and A. Samanta, Linear stability of a contaminated fluid flow down a slippery inclined plane, Phys. Rev. E **98**, 033108 (2018).

[43] A. Choudhury and A. Samanta, Linear stability of a falling film over a heated slippery plane, Phys. Rev. E **105**, 065112 (2022).

[44] A. Samanta, Modal analysis of a viscous fluid falling over a compliant wall, Proc. R. Soc. A **477**, 20210487 (2021).

[45] N. Tilton and L. Cortelezzi, Linear stability analysis of pressure-driven flows in channels with porous walls, J. Fluid Mech. **604**, 411 (2008).

[46] A. Samanta, Role of slip on the linear stability of a liquid flow through a porous channel, Phys. Fluids **29**, 094103 (2017).

[47] M. K. Smith, The mechanism for the long-wave instability in thin liquid films, J. Fluid Mech. **217**, 469 (1990).

[48] P. G. Drazin and W. H. Reid, *Hydrodynamic Stability* (Cambridge University Press, Cambridge, 1981).

[49] B. F. Farrell, Optimal excitation of perturbations in viscous shear flow, Phys. Fluids **31**, 2093 (1988).

[50] P. J. Schmid, Nonmodal stability theory, Annu. Rev. Fluid Mech. **39**, 129 (2007).

[51] L. N. Trefethen, Pseudospectra of linear operators, SIAM Rev. **39**, 383 (1997).

[52] S. C. Reddy and D. S. Henningson, Energy growth in viscous channel flows, J. Fluid Mech. **252**, 209 (1993).

[53] D. Barkley, H. M. Blackburn, and S. J. Sherwin, Direct optimal growth analysis for timesteppers, Intl. J. Numer. Methods Fluids **57**, 1435 (2008).

[54] P. J. Schmid, Linear stability theory and bypass transition in shear flows, Phys. Plasmas **7**, 1788 (2000).

[55] H. B. Squire, On the stability for three-dimensional disturbances of viscous fluid flow between parallel walls, Proc. R. Soc. A **142**, 621 (1933).

[56] S. A. Orszag, Accurate solution of the Orr-Sommerfeld stability equation, J. Fluid Mech. **50**, 689 (1971).

[57] J. P. Boyd, *Chebyshev and Fourier Spectral Methods* (Dover, Mineola, NY, 2000).